The 8th European Congress on Computational Methods in Applied Sciences and Engineering
ECCOMAS Congress 2022
5-–9 June 2022, Oslo, Norway

IMPLICIT LES OF THE TRANSONIC FLOW OVER A HIGH-PRESSURE TURBINE CASCADE USING DG SUBCELL SHOCK CAPTURING

BJOERN F. KLOSE[1], CHRISTIAN MORSBACH[2], MICHAEL BERGMANN[2] AND EDMUND KÜGELER[2]

[1] Institute of Test and Simulation for Gas Turbines
German Aerospace Center (DLR)
Am Technologiezentrum 5, 86159 Augsburg, Germany
e-mail: bjoern.klose@dlr.de

[2] Institute of Propulsion Technology
German Aerospace Center (DLR)
Linder Höhe, Cologne 51147, Germany

Key words: discontinuous Galerkin, spectral element method, shock capturing

Abstract. Implicit large-eddy simulations of the high-pressure turbine cascade VKI-LS89 under transonic operating conditions using a high-order accurate discontinuous Galerkin spectral element method are presented. The subcell shock capturing method by Hennemann et al. [1] is investigated and compared against simulations with artificial viscosity. Additionally, the effect of laminar and turbulent inflow conditions are validated against numerical and experimental results from literature. This analysis shows that the subcell-shock-capturing method performs well by effectively reducing spurious oscillations across the shock front and acoustic waves while leaving the rest of the solution domain unaffected.

1 INTRODUCTION

Scale-resolving simulations are an integral part in the validation of lower-cost computational fluid dynamics (CFD) methods and, with increasing computational resources, are also becoming an attractive tool for the design process in modern-day turbomachinery. Because such flows are typically at high Reynolds numbers, possibly transonic and strongly affected by the incoming turbulence levels, agreement of experimental and numerical results can be challenging [2, 3]. Among the numerical methods used for these high-fidelity large-eddy simulations (LES), high-order spectral methods, and in particular the discontinuous Galerkin spectral element method (DGSEM), have become popular, as they feature reduced dispersion and dissipation errors over lower-order schemes [4, 5]. The high-order polynomial approximations that spectral methods are based on, however, make this family of schemes susceptible to non-physical Gibbs-type oscillations at steep gradients or discontinuities such as shock waves.

The development of shock capturing methods tailored for the SEM framework is an active area of research with a variety of different schemes being proposed in literature [6, 7, 8]. A popular approach is the explicit addition of artificial viscosity (AV) to the system and thereby

diffusing steep gradients and eliminating spurious oscillations [9]. Persson & Peraire [6] first adapted this method for DG schemes and applied the AV as an element-wise constant quantity that scales with a smoothness-depending shock sensor. They further demonstrated that AV can either be applied via an additional Laplacian diffusion operator or added as physical viscosity and incorporated through a viscous flux formulation. The AV approach was later refined by several authors, who reported improvements through smoothing of the element-wise constant AV (see e.g. [10, 11, 12]). For a more comprehensive overview of the various artificial viscosity models, we refer to the excellent review by Yu & Hesthaven [13].

While AV is effective in reducing spurious oscillations, it changes the underlying differential equation, is parameter-dependent [11] and can result in severe time-step restrictions for explicit time-integration schemes [6, 14]. A more recently developed shock-capturing method for SEM is the subcell finite volume (FV) ansatz introduced by Sonntag & Munz [8], Vilar [15] and Hennmann et al. [1]. Here, each element is divided into subcells based on the interior quadrature nodes and the fluxes are computed based on a FV operation. The novel entropy-stable approach developed by Hennemann et al. [1] seamlessly blends the inviscid FV subcell fluxes with the higher-order split-form DG ansatz, where the amount of FV in the blending operation is determined through a shock sensor based on the energy in the highest modes of the local polynomial.

In this paper, we present results from implicit LES of the transonic high-pressure turbine cascade VKI-LS89 under transonic operating conditions using a high-order accurate discontinuous Galerkin spectral element method with subcell FV shock capturing. The scheme is tested for laminar inflow conditions and results are compared to an AV-based approach, as well as validated against numerical and experimental results from literature. In addition, first results of a refined simulation with turbulent inflow conditions are presented, as well as a frequency analysis of the dominant modes using spectral proper orthogonal decomposition (SPOD). The transonic VKI-LS89 high-pressure turbine cascade is a well-suited test case for the performance of numerical tools given the plethora of numerical references available in literature (see e.g. [16, 17, 2, 3]). The subcell-shock-capturing method is shown to perform well by more effectively reducing spurious oscillations across the shock front compared to the AV approach.

In the following chapter, we introduce the numerical scheme and provide details on the implementation of the shock-capturing method. Tests of the schemes on the Sod shock tube case are discussed next and the high-pressure turbine simulations are presented hereinafter. Conclusions are reserved for the last chapter.

2 METHODOLOGY

The simulations are conducted with the DLR turbomachinery code *TRACE* to solve the compressible Navier-Stokes equations in three dimensions. The spatial domain is discretized with a discontinuous Galerkin spectral element method, which a high-order method based on a local polynomial ansatz and extensively described and tested in [18, 19, 20].

2.1 Governing equations

We solve the compressible Navier-Stokes equations in three space dimensions, given by

$$\frac{\partial \mathbf{q}}{\partial t} + \nabla_x \cdot \mathbf{F}(\mathbf{q}, \nabla_x \mathbf{q}) = 0, \tag{1}$$

where $\mathbf{q} = [\rho, \rho u, \rho v, \rho w, \rho E]^T$ is the vector of conserved variables, $\mathbf{F}$ is the flux vector and ∇_x is the gradient operator. The flux vector can be decomposed into advective (a) and viscous (v) fluxes, $\mathbf{F} = \mathbf{F}^a(\mathbf{q}) - \mathbf{F}^v(\mathbf{q}, \nabla_x \mathbf{q})$, which are given by

$$\mathbf{F}_i^a = \begin{bmatrix} \rho u_i \\ \rho u_1 u_i + \delta_{1i} p \\ \rho u_2 u_i + \delta_{3i} p \\ \rho u_3 u_i + \delta_{2i} p \\ (\rho E + p) u_i \end{bmatrix}, \qquad \mathbf{F}_i^v = \begin{bmatrix} 0 \\ \tau_{1i} \\ \tau_{2i} \\ \tau_{3i} \\ \tau_{ij} u_j - q_i \end{bmatrix}, \qquad i = 1, 2, 3. \tag{2}$$

Here, the index i refers to the component of the Cartesian coordinates, ρ is the density, u_i are the components of the velocity vector, p is the pressure, E is the specific total energy, τ_{ij} are the components of the shear stress tensor and q_i is the heat flux vector. The system of equations is closed by the equation of state for ideal gases, $\rho E = p/(\gamma - 1) + \rho(\mathbf{u} \cdot \mathbf{u})/2$ with $\gamma = 1.4$ being the ratio of specific heats. A summation over repeated indices is assumed for equation (2).

2.2 Discontinuous Galerkin spectral element method

A DGSEM scheme is used for the spatial discretization of the system (1). Here, the computational domain $\mathcal{T}_h$ is divided into K non-overlapping hexahedral subelements $\mathcal{D}$: $\mathcal{T}_h = \bigcup_{i=1}^{K} \mathcal{D}_i$, where the solution and fluxes are approximated on an N^{th} order polynomial basis within each element. By mapping each element from the physical space in Cartesian coordinates $\mathbf{x} = (x, y, z)$ to a reference element in computational space $E = [0, 1]^3$ with generalized coordinates $\boldsymbol{\xi} = (\xi, \eta, \zeta)$, the governing equations (1) are transformed to

$$J \frac{\partial \mathbf{q}}{\partial t} + \nabla_\xi \cdot \tilde{\mathbf{F}}(\mathbf{q}, \nabla_x \mathbf{q}) = 0, \tag{3}$$

where $J(\boldsymbol{\xi})$ is the determinant of the Jacobian $\partial \mathbf{x}/\partial \boldsymbol{\xi}$ and $\tilde{\mathbf{F}}$ is the contravariant flux [21].

In the DGSEM, the solution vector $\mathbf{q}$ is approximated by piecewise polynomials, without enforcing continuity over the element interfaces. The polynomial expansion of $\mathbf{q}$ within each element is defined as

$$\mathbf{q}_h(\boldsymbol{\xi}, t) = \sum_{i=0}^{N} \sum_{j=0}^{N} \sum_{k=0}^{N} \mathbf{q}_{ijk}(t) \ell_i^N(\xi) \ell_j^N(\eta) \ell_k^N(\zeta), \tag{4}$$

where $\mathbf{q}_h$ is the polynomial approximation of q and the basis is formed by a set of Lagrange interpolating polynomials of degree N,

$$\ell_j^N(\xi) = \prod_{\substack{i=0 \\ i \neq j}}^{N} \frac{\xi - \xi_i}{\xi_j - \xi_i}. \tag{5}$$

By multiplying (3) with a test function $\phi^N = \ell_i^N(\xi) \ell_j^N(\eta) \ell_k^N(\zeta)$, which follows the same polynomial expansion as our solution (4), and integrating the resulting system by parts, the final DGSEM approximation reads

$$\int_{D_K} J \frac{\partial \mathbf{q_h}}{\partial t} \phi^N d\boldsymbol{\xi} + \int_{\partial D_K} (\tilde{\mathbf{F}}^{*,a} - \tilde{\mathbf{F}}^{*,v}) \phi^N d\mathbf{S} - \int_{D_K} \tilde{\mathbf{F}}(\mathbf{q}_h, \nabla_x \mathbf{q}_h) \cdot \nabla_\xi \phi^N d\boldsymbol{\xi} = 0. \tag{6}$$

Here, $\tilde{\mathbf{F}}^{*,a}$ and $\tilde{\mathbf{F}}^{*,v}$ are the advective and viscous numerical fluxes at the element interface, which are a function of the left and right states. The numerical fluxes are computed based on an approximate Riemann solver by Roe [22] for the advective part and the Bassy-Rebay-1 (BR1) scheme [23] for the viscous part.

A nodal-collocation approach, where the integration and quadrature points are both taken to be the Legendre-Gauss-Lobatto nodes, is applied in this work and yields an efficient numerical scheme with diagonal mass matrix [21].

We obtain the semi-discrete formulation of the high-order scheme by approximating the integrals in (6) with quadrature and write the DGSEM scheme (given for one dimension only) for the i-th node as:

$$J_i \partial_t \mathbf{q}_i + \left(\frac{\delta_{iN}}{w_N} \left[\tilde{\mathbf{F}}^* - \tilde{\mathbf{F}} \right]_N - \frac{\delta_{i0}}{w_0} \left[\tilde{\mathbf{F}}^* - \tilde{\mathbf{F}} \right]_0 \right) + \sum_{m=0}^{N} D_{im} \tilde{\mathbf{F}}_m = 0, \tag{7}$$

where $D_{ij} = \ell'_j(\xi_i)$ is the derivative matrix and w_i quadrature weights. With the summation-by-parts property of the volume flux operator in (7), Fischer et al. [24] and Carpenter et al. [25] showed that the term can be rewritten in the form

$$\sum_{m=0}^{N} D_{im} \tilde{\mathbf{F}}_m = 2 \sum_{m=0}^{N} D_{im} \tilde{\mathbf{F}}^{\#}_{(i,m)}, \tag{8}$$

which can be used with any symmetric and consistent two-point flux function.

This split-form approximation of the advective fluxes can be tailored to yield a scheme that accounts for numerical errors arising from the non-linearity of the fluxes and the limited precision of integration [26, 27]. Specifically, we employ the kinetic-energy conserving two-point fluxes by Kennedy & Gruber [28] in this work. The system (7) is advanced in time using an explicit Runge-Kutta scheme. For more details on the scheme, we refer the interested reader to Bergmann et al. [18, 20], as well as to Kopriva [21].

2.3 Subcell FV blending and artifical viscosity

2.3.1 The shock sensor

Both AV and subcell FV blending base the amount of diffusion on the strength of a shock sensor. In this work, we employ the sensor introduced by Persson & Peraire [6] and modified by Hennemann et al. [1], which relates the energy contained in the highest two modes of the polynomial to its total energy:

$$\mathbb{E} = \max \left(\frac{m_N^2}{\sum_{j=0}^{N} m_j^2}, \frac{m_{N-1}^2}{\sum_{j=0}^{N-1} m_j^2} \right). \tag{9}$$

Here, m_j are the modal coefficients of the polynomial.

The weighting function is then defined according to Hennemann et al. [1]:

$$\alpha = \left(1 + \exp\left(\frac{-s}{\mathbb{T}} (\mathbb{E} - \mathbb{T}) \right) \right)^{-1}, \tag{10}$$

where $\mathbb{T}(N) = 0.5 \cdot 10^{-1.8(N+1)^{1/4}}$, $s \approx 9.21$, N is the polynomial order and the indicator variable is chosen to be the product of pressure and density $p \cdot \rho$.

The sensor is applied to both, AV and FV-blending likewise and results in element-wise constant viscosities and blending constants respectively. To avoid large jumps to the next element, the local weights are diffused through an averaging operation between adjacent cells.

2.3.2 Artificial viscosity

Following Persson & Peraire [6], we introduce the artificial viscosity ε via a Laplace operator into the conservation laws

$$\frac{\partial \mathbf{q}}{\partial t} + \nabla_x \cdot \mathbf{F}(\mathbf{q}, \nabla_x \mathbf{q}) = \nabla_x \cdot (\varepsilon \nabla_x \mathbf{q}) = \nabla_x \cdot \mathbf{F}^{av}, \tag{11}$$

where we have defined the AV flux as

$$\mathbf{F}_i^{av} = \varepsilon \begin{bmatrix} \partial_i \rho \\ \partial_i \rho u \\ \partial_i \rho v \\ \partial_i \rho w \\ \partial_i \rho E \end{bmatrix}, i = 1, 2, 3. \tag{12}$$

and add it to the physical viscous flux before applying the divergence operation: $\mathbf{F}_i^{v,total} = \mathbf{F}_i^v + \mathbf{F}_i^{av}$.

The AV is scaled with the shock sensor (10) and acts only on regions in the field that exhibit strong polynomial oscillations, such that $\varepsilon = \alpha \cdot \varepsilon_{max}$. The maximum amount of AV is governed by the time step size, where we require that $\Delta t_{visc} \geq \Delta t_{inv}$ to avoid numerical instabilities imposed by the viscous time step limit:

$$\varepsilon_{max} \propto J \frac{1}{2N+1} \frac{\sum_{i=1}^{3} |J\mathbf{a}^i \cdot \mathbf{u}| + a\|J\mathbf{a}^i\|}{\sum_{i=1}^{3} \|J\mathbf{a}^i\|^2}. \tag{13}$$

Here, $\mathbf{a}^i = \nabla \xi^i$ are the contravariant basis vectors where again $\boldsymbol{\xi} = (\xi, \eta, \zeta) = (\xi^1, \xi^2, \xi^3)$ [21], a is the speed of sound and $|\cdot|$ and $\|\cdot\|$ refer to the L^1 and L^2 norms respectively. A tuning constant C can be added to (13) to scale the AV.

2.3.3 Subcell FV blending

We start from the inviscid conservation law in the general form $\partial_t \mathbf{q} + \mathbf{R}(\mathbf{q}) = 0$ and define the hybrid DG-FV scheme as a blending of the advective residual operator of the high-order DG ansatz ($\mathbf{R}^{DG}$) and the low-order FV approach ($\mathbf{R}^{FV}$):

$$\frac{\partial \mathbf{q}}{\partial t} + \alpha \mathbf{R}^{FV}(\mathbf{q}) + (1-\alpha)\mathbf{R}^{DG}(\mathbf{q}) = 0, \tag{14}$$

where again $\alpha \in [0, 1]$ is the blending factor based on the shock indicator (10).

Following Hennemann et al. [1], the semi-discrete low-order FV approximation of the conservation law on the subcell grid is given as

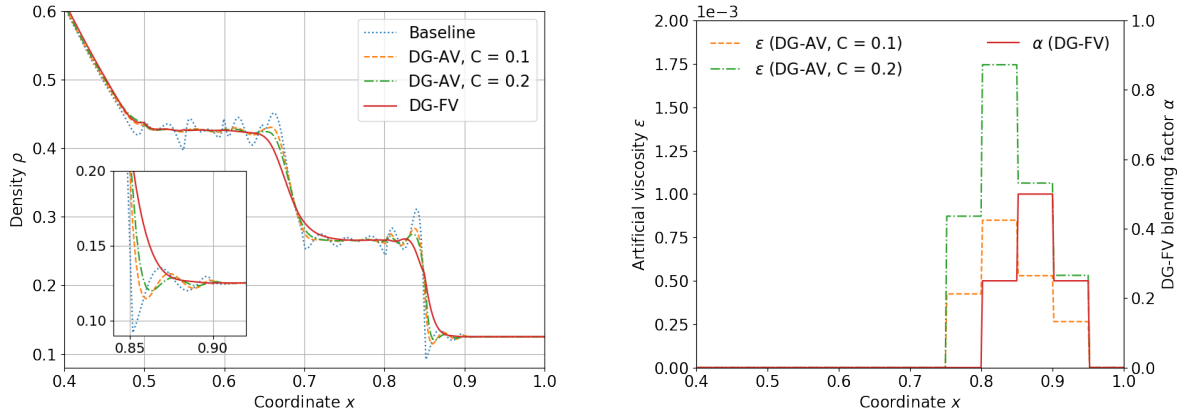

(a) Density

(b) AV & subcell FV blending factor

Figure 1: Sod shock tube problem at time $t = 0.2$. Comparison of density (a) and amount of AV & subcell FV blending (b) for the baseline DGSEM, subcell FV blending (DG-FV) and DG-AV scheme with different scaling constants.

$$J_i \partial_t \mathbf{q}_i + \frac{1}{w_i} \left[\tilde{\mathbf{F}}^*_{i,i+1} - \tilde{\mathbf{F}}^*_{i-1,i} \right] = 0, \tag{15}$$

with the nodal values $\mathbf{q}_i$ representing the mean values within the cells and $\tilde{\mathbf{F}}^*_{i,i+1} = \tilde{\mathbf{F}}^*(\mathbf{q}_i, \mathbf{q}_{i+1})$ the interface flux between the subcells i and $i+1$. For further details on the properties and the implementation of the DG-FV blending scheme, we refer to the paper by Hennemann et al. [1].

3 SOD SHOCK TUBE

We compare the subcell FV blending scheme to the AV variant and the baseline DGSEM for the solution of the one-dimensional Sod shock tube problem [29] in Figure 1. The domain is discretized with 20 elements and all simulations are run with a constant polynomial order of $N = 5$ and non-dimensional time step of 1.5×10^{-3} until $t = 0.2$. The two-point flux formulation by Kennedy & Gruber [28] is applied to the convective terms and the solution is advanced in time using an explicit fourth-order Runge-Kutta scheme.

Although numerically stable, the baseline DGSEM shows large, spurious density oscillations which are damped by both, the AV and the subcell FV variants. The subcell FV most effectively reduces the spurious overshoots among the shock capturing schemes, while the solutions from the AV simulations remain weakly oscillatory for both scaling constants C (which determine the maximum amount of AV). Although larger values of C could reduce the oscillations with the AV scheme further, a smaller time step size would be required for numerical stability and increase the computational work.

4 VKI-LS89

4.1 Numerical setup

For all simulations, the DGSEM is used with Legendre-Gauss-Lobatto (LGL) quadrature nodes and kinetic-energy conserving Kennedy-Gruber two-point fluxes. A constant polynomial order of $N = 5$ is used in all elements and yields a 6^{th} order accurate scheme. The solution is advanced in time with an explicit 3rd-order Runge-Kutta scheme and a constant time step of $\Delta t^* = \Delta t \cdot U_{out}/c = 3.9 \times 10^{-6}$, where $c = 0.067647$m is the chord length and U_{out} is the flux-averaged outlet velocity.

A Riemann boundary condition is applied at the inlet and a non-reflecting BC at the outlet [30], while periodic boundaries are set at the pitch- and spanwise domain faces. For the simulation with turbulent inflow, the synthetic turbulence generator by Shur et al. [31] is employed with turbulence levels of 6% and a length scale of 3.19mm (see Matha et al. [32] for more details). In addition to the non-uniform distribution of the LGL nodes, the collocation points are clustered towards the wall based on the inner-cell stretching method introduced by Hindenlang et al. [33] to further increase the near-wall resolution. The averaged non-dimensional cell sizes are $(\overline{\Delta\xi^+}, \overline{\Delta\eta^+}, \overline{\Delta\zeta^+}) = (63, 0.7, 39)$ and are computed from the element size normalized by the polynomial order ($\square^+ = \square_e^+/N$). ξ, η and ζ refer to the streamwise, normal and spanwise directions. While the values indicate that we only coarsely resolve the flow, high-order schemes generally allow for larger cell sizes compared to classical lower-order FV methods [34] and Alhawwary & Wang [35] hinted that LES with comparable cell spacings can still produce good results.

The DG-FV simulations are initialized from a precursor RANS solution and the DG-AV is restarted from snapshot of the DG-FV (laminar) case. The tuning constant for the DG-AV simulation is set to 0.2. A summary of the simulation parameters is given in table 4.1. We note

Table 1: Overview of simulations. AV = artificial viscosity, DGFV = DG-FV subcell blending, DOF = degrees of freedom (high-order grid points), T_{stat} = statistics interval, $t_{ref} = c/U_{out}$.

Case:	DG-AV	DG-FV	DG-FV-turb
Re_{out}	1.136×10^6	1.135×10^6	1.134×10^6
Ma_{out}	0.915	0.915	0.911
$p_{t,in}$	1.828×10^5 Pa	1.828×10^5 Pa	1.828×10^5 Pa
$T_{t,in}$	413.3K	413.3K	413.3K
T_{wall}	301.15K	301.15K	301.15K
p_{out}	1.03×10^5 Pa	1.03×10^5	1.034×10^5
Shock capturing	artificial viscosity	FV subcell blending	FV subcell blending
Inlet turbulence	0%	0%	6%
L_z	$0.1c$	$0.1c$	$0.148c$
Polynomial order	5	5	5
DOF	69.8×10^6	69.8×10^6	111.6×10^6
T_{stat}/t_{ref}	5.0	7.7	7.4

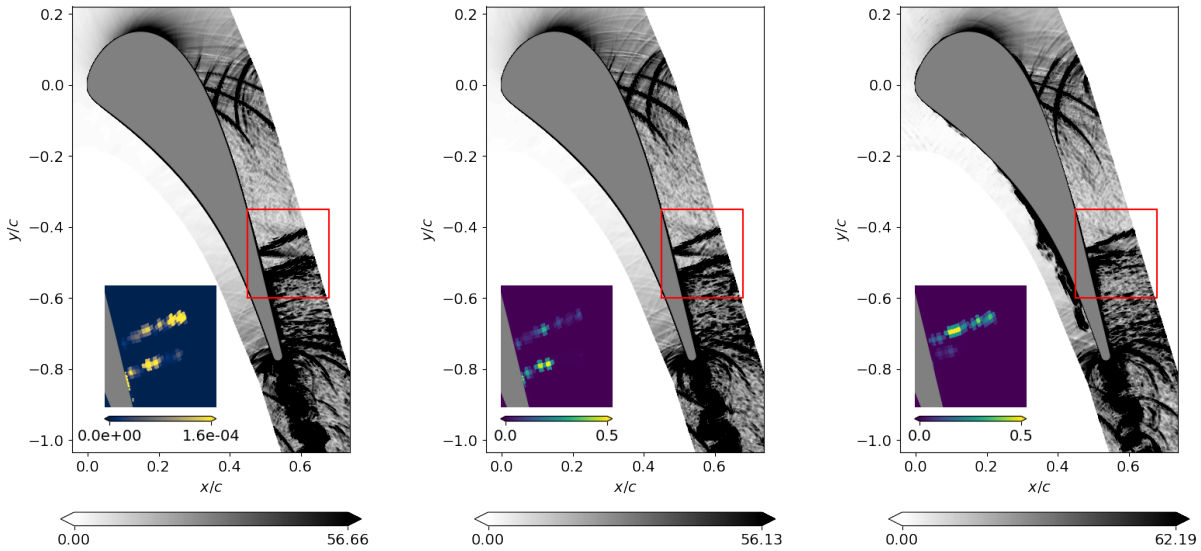

(a) DG-AV (b) DG-FV (c) DG-FV-turb

Figure 2: Contour plots of numerical schlieren ($\|\nabla\rho\|$) for DG-AV (a), DG-FV (b) and DG-FV-turb (c). The subplots show the local amount of AV (a) and the blending weights (b, c) at the location indicated by the red box.

that the dimensions of the computational domain for the DG-FV-turb case are slightly different to closely match the setup by Dupuy et al. [2].

4.2 Results

In the following section, we describe and compare the data of LES conducted with the DG-AV and the DG-FV scheme and compare them to results from literature. The frequency analysis in the subsequent part then only discusses results obtained with DG-FV and laminar inflow.

4.2.1 Comparison DG-AV and DG-FV: flow topology and surface coefficients

We visualize the instantaneous flow field through numerical schlieren images ($\|\nabla\rho\|$) for the three cases DG-AV, DG-FV and DG-FV-turb in Figure 2. The cases with laminar inflow are characterized by two quasi-steady shocks on the suction side of the blade which induce boundary layer separation and transition to turbulence, thereby enclosing a laminar separation bubble (LSB) between the shock waves as indicated by the region of negative skin friction $\overline{c_f}$ in Figure 3 (a). Acoustic waves are generated by the shedding of Von-Karman vortices from the trailing edge, which travel upstream within the subsonic region until they merge with the second shock or impinge on the suction side on the next (pitchwise) blade row. The visible differences between the DG-FV and DG-AV cases are, not surprisingly, limited to the shock region, as both methods use the same shock indicator function. A stronger overshoot of the skin friction coefficient in case of the DG-AV simulation suggests that the gradients are less diffused and result in a more oscillatory solution compared to the DG-FV simulation.

No negative values are encountered in the time- and space-averaged skin friction coefficient

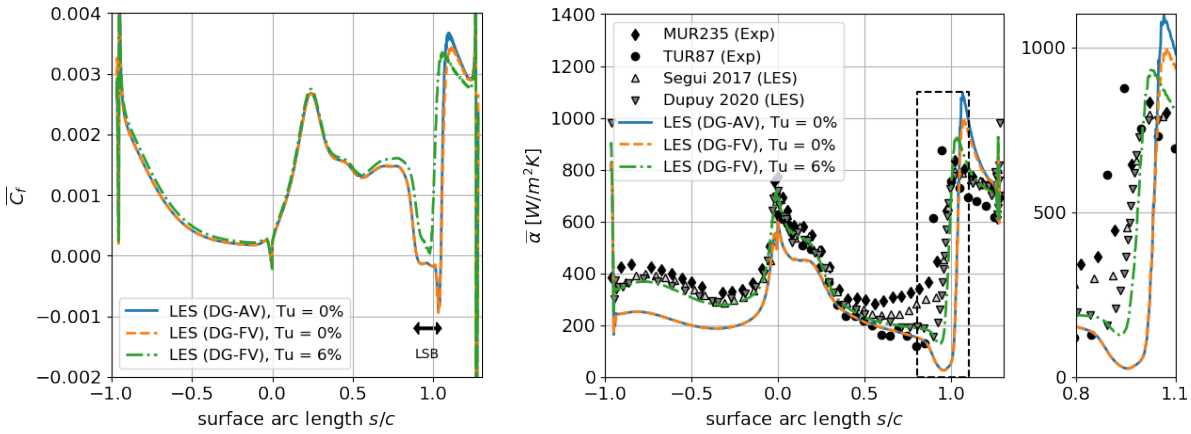

(a) Skin friction coefficient

(b) Heat transfer coefficient

Figure 3: Comparison of the time- and space-averaged skin friction coefficient $\overline{c_f}$ (a) and heat transfer coefficients $\overline{\alpha}$ (b) for DG-AV and DG-FV with laminar inflow, as well as DG-FV with turbulent inflow condition (detail plot of $\overline{\alpha}$ indicated by dashed box). Experimental reference data MUR235 by Arts et al. [36] and TUR87 by Cação Ferreira [3]. LES results by Segui [17] and Dupuy et al. [2].

for the case with turbulent inflow (DG-FV-turb), suggesting that it does not feature a LSB past the first shock, as the formation of the bubble is impeded by the incoming turbulent structures. This has also been inferred by Dupuy et al. [2], who attributed the destabilization of the LSB to the production of turbulent spots upstream of the shock, such that backflow only occurs locally. Time-resolved data further shows that the second, downstream shock is not steady - as is the case for laminar inflow - but intermittently moves upstream until it merges with the first shock. Following Dupuy et al. [2], we assume this is caused by an intermittend LSB, but further work is required to investigate the phenomenon.

We compare the time- and space-averaged heat transfer coefficient $\overline{\alpha}$ of all three simulations to the experimental campaigns by Arts et al. [36] and Cação Ferreira [3], as well as to the LES by Segui [17] and Dupuy et al. [2] in Figure 3 (b). While none of the simulations match the MUR235 operating point by Arts et al. [36], the DG-FV-turb closely aligns with the LES by Dupuy et al. [2] and also shows partial agreement with the TUR87 experiments by Cação Ferreira [3]. The main differences with the very highly resolved LES by Segui [17] is the lack of the plateau in the heat transfer coefficient upstream of the shock, which indicates that the DG-FV-turb simulation lacks the production of turbulent spots [2]. The absence of the plateau in the more recent TUR87 experiments, however, highlights that the *true* solution is still unclear while underlining the sensitive nature of the boundary layer transition of the VKI-LS89.

The cases with laminar inflow (DG-AV and DG-FV) show a stronger dip in the heat transfer coefficient at the location of the LSB and overall lower values over the pressure side, rooted in the less effective heat transfer of laminar flow. As was the case with the skin friction coefficient, the DG-AV shows a stronger overshoot past the shock. While the limited diffusion of the DG-AV scheme could be the cause, another explanation is offered by Cação Ferreira [3], who has suggested that the AV can decrease the effective Reynolds number and increase the thermal conductivity, thereby resulting in a higher heat transfer coefficient.

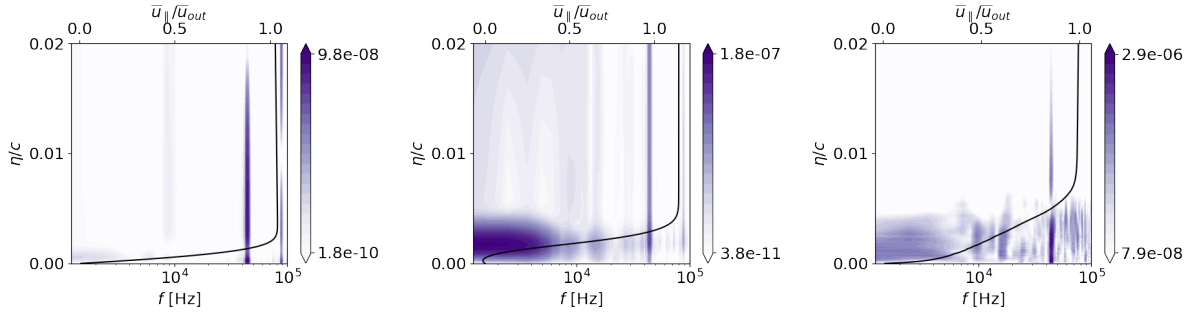

(a) Probe 1 (b) Probe 2 (c) Probe 3

Figure 4: Power spectral densities of $u_\parallel/\|u_{out}\|[\mathrm{Hz}^{-1}]$ over the wall-normal coordinate η for three probe locations. The contours are on logarithmic scale.

4.2.2 Frequency analysis

We conduct a frequency analysis of the DG-FV simulation to identify the dominant modes that occur naturally in the unperturbed flow. The power spectral density (PSD) of the wall-tangential velocity $u_\parallel$ from time-resolved boundary layer probes in the laminar flow region upstream of the shock (Probe 1), as well as directly around the two shocks (Probe 2 & Probe 3) are computed using Welch's method and plotted over the wall-normal coordinate in Figure 4. The spatial correlation of the modes is visualized by conducting a SPOD of 361 snapshots (FFT samples per block: $N_{FFT} = 128$ and overlap of 50%) of 2D slices along the centerline by employing the algorithm published by Towne et al. [37] and Schmidt & Towne [38], with an implementation available under the PYTHON package `https://pypi.org/project/pyspod/`. The input variables are chosen to be the velocity components $u_\parallel$, $u_\perp$ (normal velocity) and w and hence the SPOD is calculated with respect to the turbulent kinetic energy norm [39]. In Figure 5 (a), the mode energy is plotted over the frequency, while Figure 5 (b–d) show the contours of the first mode at frequencies of 8.3 kHz, 43.8 kHz and 87.5 kHz respectively.

The upstream probe (Figure 4a) shows two distinct peaks in the frequency range of 40 kHz to 47 kHz and at a higher harmonic of 86 kHz to 92 kHz, as well as a weaker peak at 8 kHz – 10 kHz. These peaks are also visible in the mode energy spectrum in Figure 5 (a), confirming that the SPOD complements the PSD analysis of the boundary layer probes. At 8.3 kHz, the mode highlights the wall-tangential movement of the shock-LSB system in-phase with a larger-scale swinging of the wake (Figure 5a) and the corresponding displacement of fluid. The mode at 43.8 kHz (Figure 5c) corresponds to the Von-Karmann vortex shedding at the trailing edge, as highlighted by the wake pattern of the SPOD mode, and matches the vortex shedding frequency of 43 kHz reported by Segui [17] for the MUR129 operating point. Movement of the shock itself is, however, not observed at this frequency. At the higher harmonic (87.5 kHz, Figure 5d), the SPOD shows an active mode in the turbulent shear layer in addition to the wake mode. This implies that while the shock movement is not directly linked with the trailing-edge shedding, the vortices generated from the shock-induced LSB are at least partially correlated to the primary Von-Karman shedding.

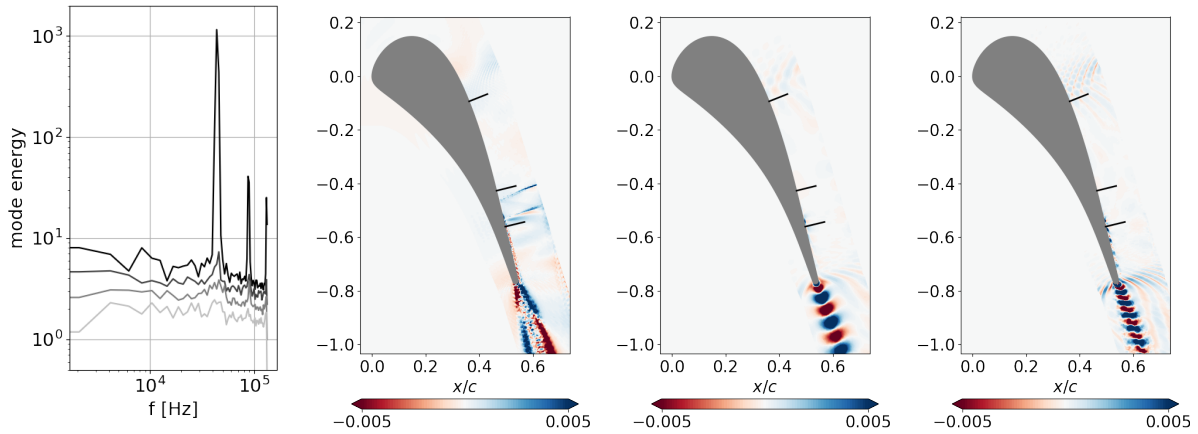

(a) mode energy (b) $f = 8.3$ kHz (c) $f = 43.8$ kHz (d) $f = 87.5$ kHz

Figure 5: (a) SPOD spectrum for modes 1 (black) to mode 4 (light gray). (b–d) Contour plots of the first SPOD modes at frequencies of 8.3 kHz (b), 43.8 kHz (c) and 87.5 kHz (d). Boundary layer probe positions indicated in black.

5 CONCLUSIONS

We have presented results from implicit large-eddy simulations of the high-pressure turbine cascade VKI-LS89 under transonic operating conditions using a high-order accurate discontinuous Galerkin spectral element method with shock capturing. The subcell finite-volume shock capturing method by Hennemann et al. [1] is tested under laminar and turbulent inflow conditions and compared against a simulation with Laplacian artificial viscosity, where it is shown to more effectively reduce spurious overshoots across the shock and match experimental values more closely. A LSB embedded by two quasi-steady shocks is present for the cases with laminar inflow, while the turbulent structures for the case with inflow turbulence prevent the formation of a bubble and only a single shock is present. By conducting a frequency analysis of boundary layer probes and through SPOD of center-line slices, we have shown that shock movement occurs at a low-frequency of 8.3 kHz and is not directly correlated to the primary Von-Karman vortex shedding at the trailing edge, or a dominant higher harmonic mode. The heat transfer coefficient of the simulation with turbulent inflow closely matches the LES by Dupuy et al. [2] and partially agrees with the experiments by Cação Ferreira [3], but differences with the highly resolved LES by Segui [17] indicates that further grid refinement might be necessary as part of future work.

REFERENCES

[1] Sebastian Hennemann, Andrés M. Rueda-Ramírez, Florian J. Hindenlang, and Gregor J. Gassner. A provably entropy stable subcell shock capturing approach for high order split form DG for the compressible euler equations. *Journal of Computational Physics*, 426:109935, feb 2021.

[2] D. Dupuy, L. Gicquel, N. Odier, F. Duchaine, and T. Arts. Analysis of the effect of intermittency in a high-pressure turbine blade. *Physics of Fluids*, 32(9):095101, sep 2020.

[3] Tânia Sofia Cação Ferreira. *Boundary layer transition and convective heat transfer of the high-pressureturbine vane LS89*. PhD thesis, Universite catholique de Louvain, 2021.

[4] Z.J. Wang, Krzysztof Fidkowski, Rémi Abgrall, Francesco Bassi, Doru Caraeni, Andrew Cary, Herman Deconinck, Ralf Hartmann, Koen Hillewaert, H.T. Huynh, Norbert Kroll, Georg May, Per-Olof Persson, Bram van Leer, and Miguel Visbal. High-order CFD methods: current status and perspective. *International Journal for Numerical Methods in Fluids*, 72(8):811–845, jan 2013.

[5] Martin Kronbichler and Per-Olof Persson, editors. *Efficient High-Order Discretizations for Computational Fluid Dynamics*. Springer International Publishing, 2021.

[6] Per-Olof Persson and Jaime Peraire. Sub-cell shock capturing for discontinuous galerkin methods. In *44th AIAA Aerospace Sciences Meeting and Exhibit*. American Institute of Aeronautics and Astronautics, jan 2006.

[7] A. Chaudhuri, G.B. Jacobs, W.S. Don, H. Abbassi, and F. Mashayek. Explicit discontinuous spectral element method with entropy generation based artificial viscosity for shocked viscous flows. *Journal of Computational Physics*, 332:99–117, mar 2017.

[8] Matthias Sonntag and Claus-Dieter Munz. Efficient parallelization of a shock capturing for discontinuous galerkin methods using finite volume sub-cells. *Journal of Scientific Computing*, 70(3):1262–1289, sep 2016.

[9] J. VonNeumann and R. D. Richtmyer. A method for the numerical calculation of hydrodynamic shocks. *Journal of Applied Physics*, 21(3):232–237, mar 1950.

[10] Garrett E. Barter and David L. Darmofal. Shock capturing with PDE-based artificial viscosity for DGFEM: Part i. formulation. *Journal of Computational Physics*, 229(5):1810–1827, mar 2010.

[11] A. Klöckner, T. Warburton, and J. S. Hesthaven. Viscous shock capturing in a time-explicit discontinuous galerkin method. *Mathematical Modelling of Natural Phenomena*, 6(3):57–83, 2011.

[12] Per-Olof Persson. Shock capturing for high-order discontinuous galerkin simulation of transient flow problems. In *21st AIAA Computational Fluid Dynamics Conference*. American Institute of Aeronautics and Astronautics, jun 2013.

[13] Jian Yu and Jan S. Hesthaven. A study of several artificial viscosity models within the discontinuous galerkin framework. *Communications in Computational Physics*, 27(5):1309–1343, jun 2020.

[14] C. Altmann, A. Taube, G. Gassner, F. Lörcher, and C.-D. Munz. Shock detection and limiting strategies for high order discontinuous galerkin schemes. In *Shock Waves*, pages 1053–1058. Springer Berlin Heidelberg, 2009.

[15] François Vilar. A posteriori correction of high-order discontinuous galerkin scheme through subcell finite volume formulation and flux reconstruction. *Journal of Computational Physics*, 387:245–279, jun 2019.

[16] E. Collado Morata, N. Gourdain, F. Duchaine, and L.Y.M. Gicquel. Effects of free-stream turbulence on high pressure turbine blade heat transfer predicted by structured and unstructured LES. *International Journal of Heat and Mass Transfer*, 55(21-22):5754–5768, oct 2012.

[17] Luis Miguel Segui. *Multiphysics coupled simulations of gas turbines*. PhD thesis, Université de Toulouse, 2017.

[18] Michael Bergmann, Rebecca Gölden, and Christian Morsbach. Numerical investigation of split form nodal discontinuous galerkin schemes for the implicit les of a turbulent channel flow. In *Proceedings of the 7th European Conference on Computational Fluid Dynamics*, 2018.

[19] M. Bergmann, C. Morsbach, and M. Franke. Implicit LES of a turbulent channel flow with high-order discontinuous galerkin and finite volume discretization. In *Direct and Large-Eddy Simulation XI*, pages 61–67. Springer International Publishing, 2019.

[20] M. Bergmann, C. Morsbach, and G. Ashcroft. Assessment of split form nodal discontinuous galerkin schemes for the LES of a low pressure turbine profile. In *ERCOFTAC Series*, pages 365–371. Springer International Publishing, 2020.

[21] David A. Kopriva. *Implementing Spectral Methods for Partial Differential Equations*. Springer Netherlands, 2009.

[22] P.L Roe. Approximate riemann solvers, parameter vectors, and difference schemes. *Journal of Computational Physics*, 43(2):357–372, oct 1981.

[23] F. Bassi and S. Rebay. A high-order accurate discontinuous finite element method for the numerical solution of the compressible navier–stokes equations. *Journal of Computational Physics*, 131(2):267–279, mar 1997.

[24] Travis C. Fisher and Mark H. Carpenter. High-order entropy stable finite difference schemes for nonlinear conservation laws: Finite domains. *Journal of Computational Physics*, 252:518–557, nov 2013.

[25] Mark H. Carpenter, Travis C. Fisher, Eric J. Nielsen, and Steven H. Frankel. Entropy stable spectral collocation schemes for the navier–stokes equations: Discontinuous interfaces. *SIAM Journal on Scientific Computing*, 36(5):B835–B867, jan 2014.

[26] Gregor J. Gassner, Andrew R. Winters, and David A. Kopriva. Split form nodal discontinuous galerkin schemes with summation-by-parts property for the compressible euler equations. *Journal of Computational Physics*, 327:39–66, dec 2016.

[27] Andrew R. Winters, Rodrigo C. Moura, Gianmarco Mengaldo, Gregor J. Gassner, Stefanie Walch, Joaquim Peiro, and Spencer J. Sherwin. A comparative study on polynomial dealiasing and split form discontinuous galerkin schemes for under-resolved turbulence computations. *Journal of Computational Physics*, 372:1–21, nov 2018.

[28] Christopher A. Kennedy and Andrea Gruber. Reduced aliasing formulations of the convective terms within the navier–stokes equations for a compressible fluid. *Journal of Computational Physics*, 227(3):1676–1700, jan 2008.

[29] Gary A Sod. A survey of several finite difference methods for systems of nonlinear hyperbolic conservation laws. *Journal of Computational Physics*, 27(1):1–31, apr 1978.

[30] Daniel Schlüß, Christian Frey, and Graham Ashcroft. Consistent non-reflecting boundary conditions for both steady and unsteady flow simulations in turbomachinery applications. In *ECCOMAS Congress 2016 VII European Congress on Computational Methods in Applied Sciences and Engineering, Crete Island, Greece*, 2016.

[31] Michael L. Shur, Philippe R. Spalart, Michael K. Strelets, and Andrey K. Travin. Synthetic turbulence generators for RANS-LES interfaces in zonal simulations of aerodynamic and aeroacoustic problems. *Flow, Turbulence and Combustion*, 93(1):63–92, may 2014.

[32] Marcel Matha, Christian Morsbach, and Michael Bergmann. A comparison of methods for introducing synthetic turbulence. *7th European Conference on Computational Fluid Dynamics*, 2018.

[33] Florian J. Hindenlang, Gregor J. Gassner, and Claus-Dieter Munz. Improving the accuracy of discontinuous galerkin schemes at boundary layers. *International Journal for Numerical Methods in Fluids*, 75(6):385–402, mar 2014.

[34] Nicholas J. Georgiadis, Donald P. Rizzetta, and Christer Fureby. Large-eddy simulation: Current capabilities, recommended practices, and future research. *AIAA Journal*, 48(8):1772–1784, aug 2010.

[35] Mohammad Alhawwary and Z.J. Wang. On the mesh resolution of industrial LES based on the DNS of flow over the t106c turbine. *Advances in Aerodynamics*, 1(1), dec 2019.

[36] Tony Arts, Muriel Lambert De Rouvroit, and A. W. Rutherford. Aero-thermal investigation of a highly loaded transonic linear turbine guide vane cascade: A test case for inviscid and viscous flow computations. Technical report, Von Karman Institute for Fluid Dynamics, 1990.

[37] Aaron Towne, Oliver T. Schmidt, and Tim Colonius. Spectral proper orthogonal decomposition and its relationship to dynamic mode decomposition and resolvent analysis. *Journal of Fluid Mechanics*, 847:821–867, may 2018.

[38] Oliver T. Schmidt and Aaron Towne. An efficient streaming algorithm for spectral proper orthogonal decomposition. *Computer Physics Communications*, 237:98–109, apr 2019.

[39] Oliver T. Schmidt and Tim Colonius. Guide to spectral proper orthogonal decomposition. *AIAA Journal*, 58(3):1023–1033, mar 2020.